An Assessment of the Impact of ATMS and CrIS Data Assimilation on Precipitation Prediction over the Tibetan Plateau

Tong Xue[1, 2, 4], Jianjun Xu[2, 3], Zhaoyong Guan[1], Han-Ching Chen[4, 5], Long S. Chiu[4], Min Shao[6]

[1]Key Laboratory of China Education Ministry for Meteorological Disasters, Nanjing University of Information Science and Technology, Nanjing, China

[2] Guangdong Ocean University, Zhanjiang, China

[3] State Key Laboratory of Severe Weather, Chinese Academy of Meteorological Sciences, China

[4]AOES, College of Science, George Mason University, Fairfax, Virginia, USA

[5]Department of Atmospheric Sciences, National Taiwan University, Taipei, Taiwan

[6] GENRI, College of Science, George Mason University, Fairfax, Virginia, USA

Correspondence to: Jianjun Xu ,Guangdong Ocean University, Zhanjiang, China (gdouxujj@qq.com) and Han-Ching Chen, National Taiwan University, Taipei, Taiwan , (s910810909@gmail.com)

Abstract

Using the National Oceanic and Atmospheric Administration's Gridpoint Statistical Interpolation data assimilation system and the National Center for Atmospheric Research's Advanced Research Weather Research and Forecasting (WRF-ARW) regional model, the impact of assimilating advanced technology microwave sounder (ATMS) and cross-track infrared sounder (CrIS) satellite data on precipitation prediction over the Tibetan Plateau in July 2015 was evaluated. Four experiments were designed: a control experiment and three data assimilation experiments with different data sets injected: conventional data only, a combination of conventional and ATMS satellite data, and a combination of conventional and CrIS satellite data. The results showed that the monthly mean of precipitation is shifted northward in the simulations and shows an orographic bias described as an overestimation in the upwind of the mountains and an underestimation in the south of the rainbelt. The rain shadow mainly influenced prediction of the quantity of precipitation, although the main rainfall pattern was well simulated. For the first 24-hour and last 24-hour accumulated daily precipitation, the model generally overestimated the amount of precipitation, but it was underestimated in the heavy rainfall periods of 3-5, 13-16, and 22-25 July. The observed water vapor conveyance from the southeastern Tibetan Plateau was larger than in the model simulations, which induced inaccuracies in the forecast of heavy rain on 3–5 July. The data assimilation experiments, particularly the ATMS assimilation, were closer to the observations for the heavy rainfall process than the control. Overall, based on the experiments in July 2015, the satellite data assimilation improved to some extent the prediction of precipitation pattern over the Tibetan Plateau although the simulation of rainbelt without data assimilation shows the regional shifting.

Key words: Radiance data assimilation, GSI, Tibetan Plateau, Weather forecast accuracy

1. Introduction

The Tibetan Plateau (TP) is the highest and largest plateau in the world. It is located in the central Eurasian continent and stands in the middle troposphere, covering an area of approximately 2.5 million km^2. The TP has a variety of topographical features of a large terrain gradient and its steep mountains are aligned with an east-to-west arrangement. The dramatic modification caused by the rugged terrain influences the local atmospheric circulation and causes strong local convection to arise, easily inducing severe weather such as heavy rainfall, windstorms, hailstorms, and so on (Massacand et al., 1998; Gao et al., 2015). Precipitation is one of the key variables for understanding the hydrological cycle on the TP and has profound effects on the regional and global circulation that affect millions of people in the adjacent areas (Ye and Gao, 1979; Chen et al., 1985; Chambon et al., 2014; Li et al., 2014). Therefore, making accurate and long-lead weather forecasts at high temporal and spatial resolution for the TP not only has scientific significance but also addresses the urgent need for disaster prevention. However, due to the variable weather conditions and complex terrain orography, the TP remains a sparsely populated region with few conventional observation data sources, and the limited available meteorological data leads to great uncertainties in the regional weather forecasts. The continuous development of numerical weather prediction (NWP) models, such as the National Center for Atmospheric Research (NCAR)'s Advanced Research Weather and Research Forecasting (WRF-ARW) model, offer opportunities to improve regional weather forecasts in data-sparse regions. NWP models can be initialized with and laterally assimilate observation data, which is beneficial for better describing atmospheric conditions, thus keeping model results close to observations (Maussion et al., 2011).

Satellite radiance data are one of the most important observation data sources and can be directly assimilated into data assimilation models. Compared with conventional observation data, geostationary satellite data have continuous spatial and temporal coverage and polar orbiting satellites circle the earth twice a day to provide global observations of multiple meteorological variables, such as temperature, pressure, moisture, and so on. Moreover, many studies have suggested that the assimilation of satellite radiance data can substantially improve weather forecasts (Eyre, 1992; Derber and Wu, 1998; Xu et al., 2009). For longer-range prediction, satellite data are even more crucial than conventional observations (Zapotocny et al., 2008). Past studies have also indicated that the effect of assimilation of both observations and satellite products was better than only satellite data assimilation (Liu et al., 2013).However, the performance of satellite radiance assimilation in limited-area modeling systems using variational DA method is still controversial (Zou et al., 2013; Newman et al., 2015).Schwartz et al. (2012) was the first to assimilate microwave radiances with the region lacking observation stations using ensemble Kalman filter (ENKF) and the results showed that assimilating microwave radiances overall make better forecasts of Typhoon Morakot (2009). The negative influence has also appeared and it is mainly contributed to various of factors such as the influence of lateral boundary conditions within the regional domain (Warner et al., 1997) and non-uniform satellite coverage (Kazumori et al., 2013).

The advanced technology microwave sounder (ATMS) and cross-track infrared sounder (CrIS) are two instruments with high resolution onboard the Suomi National Polar-orbiting Partnership spacecraft a polar-orbiting satellite launched in 2011 with the aim to provide real-time sensor data for critical weather and climate measurements. The ATMS, a cross-track microwave scanner with 22 channels, combines most of the channels of the preceding advanced microwave sounding unit (AMSU-A) and microwave humidity sounder (MHS) to provide sounding profiles of atmospheric moisture and temperature. The CrIS is a Fourier transform spectrometer with 1305 spectral channels inherited from the high-resolution infrared radiation sounder (HIRS) to produce temperature, pressure, and moisture profiles. A previous study assimilated ATMS data in the European Centre for Medium-Range Weather Forecasts system and the results showed that the instrument had better performance than AMSU-A and MHS in the longer range over the Northern Hemisphere (Bormann et al., 2013). Nevertheless, satellite data assimilation into NWP models over the TP presents special challenges, because the limited model capability for assimilating radiance data over complex terrain with heterogeneous characteristics is still not clearly recognized. Furthermore, whether the new generation of satellite observations, such as ATMS and CrIS, can compensate for the shortage of data over the TP and effectively enhance the accuracy of forecasts remains unknown.

In this paper, we make an assessment of the impact of assimilating ATMS and CrIS radiance data for East Asia on precipitation prediction over the TP and compare the effects of different satellite data sets injected.

2. Data and Models

2.1 Data

2.1.1 Data used for the assimilation

The conventional data which is from the Global Data Assimilation System (GDAS)-prepared BUFR files (gdas1.tCCz.prepbufr.nr) is composed of a global set of surface and upper air reports operationally collected by the National Centers for Environmental Prediction (NCEP). It includes radiosondes, surface ship and buoy observations, surface observations over land, pilot balloon (pibal) winds and aircraft reports from the Global Telecommunications System (GTS), profiler and US radar derived winds, Special Sensor Microwave Imager (SSM/I) oceanic winds and atmospheric total column water (TCW) retrievals, and satellite wind data from the National Environmental Satellite Data and Information Service (NESDIS). The reports can include pressure, geopotential height, temperature, dew point temperature, wind direction and speed. (National Centers for Environmental Prediction/National Weather Service/NOAA/U.S. Department of Commerce. 2008, updated daily. *NCEP ADP Global Upper Air and Surface Weather Observations (PREPBUFR format), May 1997* - *Continuing*.)

ATMS and CrIS satellite radiance data are also from the GDAS which is in the BUFR format. All of this can be downloaded from https://www.ncdc.noaa.gov/data-access/model-data/model-datasets/global-data-assimilation-system-gdas.

2.1.2 Data used for the evaluation/verification

Observational precipitation data from the National Meteorological Information Center (NMIC) of the China Meteorological Administration (CMA) was used as the truth data for comparison with the model results. The 0.1° × 0.1° high-resolution gridded hourly China Merged Precipitation Analysis (CMPA) data gauge, which combines the CMA's rain gauge hourly data provided by more than 30,000 automatic weather stations with the National Oceanic and Atmospheric Administration (NOAA) Climate Prediction Center's Morphing (CMORPH) precipitation product (Xie & Xiong, 2011; Pan et al., 2012; Shen et al., 2014), was used for verification to evaluate the model simulation results. Considering the topographically complex terrain characterizing the TP, satellite precipitation data with very high spatial resolution is especially needed. CMORPH product makes use of the precipitation estimates technique that have been derived from low orbiter satellite microwave observations and geostationary satellite IR data with spatial propagation features. Several studies (Gao et al., 2013; Guo et al., 2014; Tong et al., 2014; Zhang et al., 2015) have compared the CMORPH data with satellite precipitation data sets in the TP area with the conclusion that CMORPH data is one of the most suitable product to use in studying precipitation over the TP. During the period from May to October 2004-2009, Tropical Rainfall Measuring Mission (TRMM) Multisatellite Precipitation Analysis real-time research 3B42 version 6 (TMPA) and CMORPH show better performance in higher correlation and lower RMSE than the Precipitation Estimation from Remotely Sensed Information using Artificial Neural Network (PERSIANN) and TMPA's real time version (TMPART) over the TP(Gao et al., 2013). Of the several merged satellite precipitation products (i.e.TMPA, PERSIANN, and the Global Satellite Mapping of Precipitation (GSMaP)), the CMORPH product with the highest resolution (8 km) can capture the afternoon-to-evening precipitation pattern (Guo et al.,2014). Tong (2014) has also compared the performance of four widely-used high resolution satellite precipitation estimates against gauge observations (the CMA data) over the TP during January 2006-December 2012. It's worth noticing that TMPA and CMORPH data had better performance in depicting precipitation timing and amount than the TMPART and PERSIANN at both the plateau and basin scale. Zhang (2015) has also made a conclusion that the high resolution CMORPH data can depict finer regional details, such as a less coherent phase pattern over the TP and better capture the features of the diurnal cycle of summer precipitation compared with TRMM 3B42.

NCEP Final Analysis (FNL) data was used through dynamic downscaling as observed moisture to illustrate the transportation of water vapor in East Asia.

2.1.3 Radiance data quality control

As the quality of the observational data is easily affected by the observation instruments, station positions, or human factors, carrying out quality control before data application is necessary (Hubbard and You, 2005). Before data assimilation, a multiple-step quality control procedure was applied to the satellite radiance data in the GSI system and preprocessed by NOAA's Satellite and Information Service (NESDIS). Besides data thinning, it can be summarized to several quality control (QC) categories in GSI to either toss the questionable observations or inflate the low confidence observations. The detailed quality control can be found in the section 8.3 radiance observation quality control in the Gridpoint Statistical Interpolation (GSI) Advanced User's Guide version 3.5 by Developmental Testbed Center (DTC) (2016). The observational number of ATMS data ranging from 53042 to 68618 in contrast to the number of CrIS data ranging from 2694048 to 3454542 are read in DA system. After the data had passed rigorous quality assessment and quality control processes, the results showed that about 23.2%-26.4%, and 1.3% and 1.6% of "good" observations related to ATMS and CrIS read data separately were retained after quality control (Fig. 2). This difference can be explained that CrIS has 1305 channel satellite radiance data, but the number of assimilated channels are significantly reduced (Table 1), the selection of redundant channel leads to some part of observation radiance data comes from the similar altitude and contains large amount of repeated information. Therefore, larger percentage of CrIS satellite radiance data than ATMS is tossed through QC steps. Figure 1(b) shows the distribution of the conventional data at 06:00 UTC on 1 July 2015, where observational data are rare in the TP. Figure 1c and 1d displays the distribution of satellite data after quality control, where there is almost complete spatial coverage in East Asia including the TP.

2.2 Models

2.2.1 WRF-ARW regional model

NCAR's WRF-ARW regional model associated with the Gridpoint Statistical Interpolation

(GSI) data assimilation system was used in this study. WRF-ARW is a fully compressible nonhydrostatic, primitive-equation, mesoscale meteorological model. As shown in Figure 1a, the model domains are two-way nested with 12 km (580 × 422) and 4 km (817 × 574) horizontal spacing. There are 51 vertical levels with a model top of 10 hPa. Figure 1 shows that D01 is set to cover most of East Asia and the subdomain (D02) inside corresponds to the Tibetan Plateau, which has a mountain–valley structure.

The physical parameterizations chosen for the forecast model in this study followed previous studies of the area (He et al., 2012; Xu et al., 2012; Zhu et al., 2014). These included the WRF-ARW Single-Moment 6-class (WSM-6) microphysics scheme, the Kain-Fritsh (KF) cumulus parameterization, the Rapid Radiative Transfer Model (RRTMG) longwave and shortwave radiation, the Yonsei University scheme (YSU) and the Noah Land Surface Model for the planetary boundary layer scheme.

The National Centers for Environmental Prediction (NCEP) global forecast system (GFS) forecast data, which has a horizontal resolution of 0.5° × 0.5° with a 6-hour interval, were used as the boundary and initial conditions for the control (CTRL) experiment, while the background fields of data assimilation experiments (DA) take advantages of the forecast product at 06:00 UTC made by CTRL. The GFS data are publicly available from https://www.ncdc.noaa.gov/data-access/model-data/model-datasets/global-forcast-system-gfs.

2.2.2 The GSI 3D-Var system and Community Radiative Transfer Model

In this study, we chose to use the GSI 3D-Var system, which is a data assimilation system that was initially developed as the next-generation analysis system based on the operational Spectral Statistical Interpolation (SSI) at NCEP (Derber and Wu, 1998).

Instead of the spectral definition of backgrounds errors in the SSI, GSI is constructed in physical space which the background errors can be represented by a non-homogeneous and anistropic gridpoint and used for both global and regional forecasts. GSI utilizes recursive filters and is designed to be a flexible system that is efficient on available parallel computing platforms (Wu et al., 2002; Purser et al., 2003a, b). The GSI 3D-Var system provides an optimal analysis through two outer iterative minimization of a prescribed function as follows:

$$\mathrm{J} = \frac{1}{2}(\mathrm{x_a} - \mathrm{x_b})^{\mathrm{T}}\mathrm{B}^{-1}(\mathrm{x_a} - \mathrm{x_b}) + \frac{1}{2}(\mathrm{H(x)} - \mathrm{O_o})^{\mathrm{T}}\mathrm{O}^{-1}(\mathrm{H(x)} - \mathrm{O_o}) \qquad (1)$$

Where $\mathrm{x_a}$ is the analysis state can be calculated by minimizing the penalty function J, $\mathrm{x_b}$ is the first guess that comes from GFS product in this article representing background model state, $\mathrm{O_o}$ are the observations including conventional observation, satellite radiance data, radar data, etc. $\mathrm{H(x)}$ is the transformation operator from the analysis variable to the form of the $\mathrm{O_o}$ error. By means of the two sources of priori data: the first guess $\mathrm{x_b}$ and the observations $\mathrm{O_o}$, the solution for the penalty function which indicates the posteriori maximum likelihood estimate of the true atmospheric state can be found. While B and O are the error estimates of $\mathrm{x_b}$ (covariance matrix of the background error) and $\mathrm{O_o}$ (covariance matrix of the observation error) respectively which are used to weight the analysis fit to individual observations (Wu et al., 2002).

The development of fast radiative transfer models has allowed for the direct assimilation of satellite infrared and microwave radiances in NWP systems (Saunders et al., 1999; Gauthier et al., 2007; Zou et al., 2011). The Community Radiative Transfer Model (CRTM) developed by the United States Joint Center for Satellite Data Assimilation (JCSDA) has been incorporated into the NCEP GSI system to rapidly calculate satellite radiances (Han, 2006; Weng, 2009). After ATMS and CrIS data are read into the GSI, simulated brightness temperature are calculated via CRTM 2.1.3 in this study. It is worth noticing that the CrIS scans a 2200km swath width (+/- 50 degrees), with 30 Earth-scene views. Each field consists of 9 fields of view, arrayed as 3x3 array of 14km diameter spots (nadir spatial resolution). (https://jointmission.gsfc. nasa.gov/cris.html). The ATMS scans a 2300km swath width with 96 Earth-scene views. The 1-2 channel of the spatial resolution of ATMS at nadir is 75km; 3-6 channel is 32km; 17-22 channel is 16km (Dong et al., 2014).

3. Method and experimental design

3.1 Method

A basic two-by two contingency table (Table 2) was generated to calculate the Bias Score (BIAS), Fraction skill Score (FSS), Equitable Threat Score (ETS), Probability of False Detection (POFD), Probability of Detection (POD), and False Alarm ratio (FAR).

The BIAS (Range: 0~∞, Perfect score: 1), which measures the ratio of the frequency of forecast events to the frequency of observed events, is defined as:

$$\mathrm{BIAS} = \frac{\mathrm{Hits+False\ alarms}}{\mathrm{Hits+Misses}} \tag{2}$$

The FSS (Range: 0~1, Perfect score: 1) introduced by Roberts and Lean (2008) is a neighborhood verification method. The FSS is defined as:

$$\mathrm{FSS} = 1 - \frac{FBS}{FBS_{ref}} \tag{3}$$

Fractions Brier Score (FBS) is presented as

$$\mathrm{FBS} = \frac{1}{N}\sum_{i=1}^{N}[F_o - F_f]^2 \tag{4}$$

Where N is the number of all grid points in the domain. F_o and F_f are the observation and forecast fractions of the sliding window at each grid point. The sliding window in this study is 100km (25 grid points). The reference Fractions Brier Score (FBS_{ref}) represent a largest possible FBS and is given as：

$$FBS_{ref} = \frac{1}{N}\left[\sum_{i=1}^{N} {F_o}^2 + \sum_{i=1}^{N} {F_f}^2\right] \tag{5}$$

The ETS (Range: -1/3~1, Perfect score: 1) computes the fraction of observed events that were correctly predicted:

$$\mathrm{ETS} = \frac{\text{Hits} - R}{\text{Hits} + \text{False alarms} + \text{Misses} - R} \tag{6}$$

where R is the random forecast coefficient, given by:

$$\mathrm{R} = \frac{(\text{Hits} + \text{False alarms})(\text{Hits} + \text{Misses})}{(\text{Hits} + \text{False alarms} + \text{Misses} + \text{Correct rejections})} \tag{7}$$

The POFD (Range: 0~1, Perfect score: 0) measures discrimination:

$$\mathrm{POFD} = \frac{\text{False alarms}}{\text{False alarms} + \text{Correct rejections}} \tag{8}$$

Similar to the POFD, the POD (Range: 0~1, Perfect score: 1) shows the hits out of total observed events:

$$\mathrm{POD} = \frac{\text{Hits}}{\text{Hits} + \text{Misses}} \tag{9}$$

The FAR (Range: 0~1, Perfect score: 0) indicates the fraction of the predicted events that did not occur:

$$\mathrm{FAR} = \frac{\text{False alarms}}{\text{Hits+False alarms}} \tag{10}$$

To compare the model simulation data with the observation data, the 4-km model grid was interpolated to observation data with 0.1°×0.1° degree grid based on linear interpolation method.

3.2 Experimental design

Four one-month-long experiments were conducted (Fig. 3). The CTRL experiment was carried out first with an initial time of 00:00 UTC and made 54 h forecasts. The data assimilation was applied on the D01 region of the output from CTRL at 06:00 UTC. The DA experiments made use of the assimilated D01 and the D02 from the CTRL at 06:00 UTC as the initial condition and made a 48 h forecast for each day. Three DA experiments were performed with a time window of 3 hours: (1) a conventional run (CONV) assimilating the conventional observation data only; (2) an ATMS radiance run (ATMS) adding the ATMS satellite radiance data to the CONV; and (3) a CrIS radiance run (CRIS) adding the CrIS satellite radiance data to the CONV.

The accumulated precipitation integrated from 06 to 30 h and 30 to 54 h are defined as the first twenty-four-hour accumulated (F24H) precipitation and last twenty-four-hour accumulated (L24H) precipitation, respectively.

4. Results

4.1 Impact of DA on the spatial fields of precipitation forecast

Figure 4 shows the spatial pattern of the monthly mean of 24-hour accumulated precipitation in July 2015. Monthly mean precipitation exhibits a decreasing south-to-north gradient. The predicted precipitation in the central and northern parts of the TP, Qaidam Basin (90°-99°E, 35°-39°N), Tarim Basin (75°-90°E, 37°-42°N), and Junggar Basin (80°-90°E, 45°-48°N) was too small to be measured (Fig. 4a, c). It was found that F24H precipitation ranged from 6.0 to 30.4 mm, while the L24H forecasts ranged from 6.0 to 29.5 mm per month. The rain shadow along the Himalayas (73°-95°E, 27°-35°N) was found in the spatial distribution of precipitation. Due to the Figure 4 (a) standing for the F24H, the first day calculated in Figure 4 (a) was during the period of 06:00 UTC 1^{st} July to 06:00 UTC 2^{nd} July and finally ended in the period of 06:00 UTC 29^{th} July to 06:00 UTC 30^{th} July. Therefore the different values in Figure 4 (a) and (c) can be explained that the Figure 4 (c) shows the L24H observed monthly mean accumulated precipitation of which the computing process are different in in two days with Figure 4 (a). The CTRL (Fig. 4b, d) mostly simulated the monthly mean rainbelt distributed along the southern and southwestern margin of the plateau, between the Himalayas in the west and the Hengduan Mountains (95°-103°E, 24°-32°N) in the east. The difference between the model simulations and observations (Fig. 5) indicated that the CTRL simulation tends to overestimate precipitation, especially in the southern and southwestern margin along the rainbelt where the altitude changes from 500 to 3000 m. The results suggested that the WRF-ARW model has limitations in simulating the precipitation in mountainous areas, which is similar to the conclusion of previous studies (He et al., 2012; Xu et al., 2012). Furthermore, we found that the precipitation is overestimated (colored red) in the upwind of the mountains along the southwestern margin. In contrast, the precipitation is underestimated in the south of the rainbelt, leading to a north–south dipole structure. This pattern results in a northward migration of the rainbelt in the simulations. The three DA experiments indicated that the assimilation of satellite radiance data can not calibrate the rain shadow effect and all experiments showed consistently gross overestimation patterns, varying from 8 to 10 mm about the monthly mean precipitation. The overall bias statistic in D02 is 0.97 mm (0.86 mm), 0.52 mm (0.70 mm), 1.08 mm (0.97 mm), and 0.98 mm (0.76 mm) CTRL, CONV, ATMS and CRIS respectively. The values in brackets are referred to L24h. This may be attributed to the physical package of WRF-ARW having an inadequate description of snow cover over the plateau surface making the error of margin more prominent (Marteau et al. 2015).

Figure 6 shows the spatial patterns according to the contingency table (Table 2) and the scatter plots, in which monthly mean 24 h rainfall over the 6 mm threshold is defined as an "event". Rainfall events occur over most of the TP area, including the northern Gangetic Plain (80°-90°E, 24°-28°N) where the elevation is lower than 3000 m, and can be well predicted with ~8–10% hits (A) and ~76–79% correct rejections (D) in the majority of the region. The false alarms (B) were spread mainly in the east of the TP, where the Bayan Har (95°E, 35°N) and Hengduan mountains are located, accounting for ~7–10%, while the misses (C) were distributed in the western plain exterior of the TP and accounted for ~5–6%. It's also evident to see the dipole pattern in the distribution of the hits and misses similar to the Figure 5. Among the four linear regression lines (bold grey lines), ATMS looks a little better than the other three experiments but has more extreme-precipitation event forecasts than the others, followed by the CTRL and CRIS, while CONV has the lowest simulation precision. The ~84-89% high percentage of hits and correct rejections events indicates that rainfall events are well predicted. Furthermore, as the false alarms were primarily located in the east of the TP in contrast to the misses in the west, this special pattern can help WRF-ARW model reduce model error in the future which means that WRF-ARW model has promising potential in TP area.

Figure 7 shows the monthly and domain average validation statistics in the TP. The differences between the four experiments for the F24H forecasts are larger than for the L24H forecasts. The ETS, FSS, and POD values all decline as the threshold increases; a higher value for these three skill scores indicates a better performance of the experiments. ATMS showed the highest FSS (Fig. 7b), ETS (Fig. 7c) and POD (Fig. 7d). CONV performed similar to the CTRL in ETS and FSS, and CRIS performed the worst. However, according to the BIAS, CONV is mostly approximately 1, which indicates the best overall relative frequencies compared with the other experiments. Through the 1–5 mm threshold, CRIS performs the largest overforecast (BIAS > 1), but it evolves to have a better performance than ATMS and CTRL through the 5–10 mm threshold. FAR and POFD results indicate that CONV performs best (0 is perfect), followed by ATMS and then CTRL and CRIS. However, POD results manifest that ATMS performs best

(1 is perfect) and CONV is worst. The different methods of forecast verification may depend on the purpose of the verification, and the results we evaluated by different methods can explain the different question we want to answer. Overall, the results reflect that DA has a positive effect on reproducing the monthly mean precipitation in the TP compared with the CTRL to varying degrees.

4.2 Impact of DA on the temporal distribution of precipitation forecast

Another measure of performance is to examine how the daily precipitation is temporally distributed (Fig. 8). It can be seen in the time series of Figure 8a that there are four observed heavy rainfall events (3.0 mm/day) during the periods of 3–5, 8-10，13–16 and 22–25 July (Fig. 8a). In general, the F24H amount of precipitation is overestimated in all three DA experiments by 20%, 40%, and 37% for CONV, ATMS, and CRIS, respectively. In contrast, of the 4 heavy rainfall periods, 3 events including 3–5, 13–16 and 22–25 July are underestimated (grey shadings). The L24H forecasts (Fig. 8b) showed a similar pattern, except that there were much smaller differences among the three DA experiments compared with the F24H forecasts. The F24H forecasts appear the one-day time lag effect compared with L24H. Because the F24H forecasts calculate the cumulative precipitation of the first 6-30 hour while the L24H forecasts represent the 30-54 hour cumulative precipitation forecasts. When all the overestimation events are considered, the CONV (blue line) experiment captured the accumulated amount of precipitation much more accurately than the other DA experiments and the ATMS (red line) performed the worst. It is usual to define the amount of 25.0 to 49.9 mm and 50 mm daily precipitation as heavy rain and rainstorm, respectively. However, due to the history data sets of the TP indicating that the days of precipitation exceeding 50 mm are few (only accounting for 0.3% of rain days) (Wei et al., 2003) and referring to previous studies (Wang et al., 2011; Zhao et al., 2015), the heavy rainfall threshold was defined as above 20 mm for the 24 h precipitation in this study. As mentioned above, the 24 h precipitation maxima surpassing 20 mm are spread in the main precipitation region, showing that the prominent geographical dependence of rainfall coincides with the threshold of heavy rainfall defined for TP areas.

Although previous studies and our results show an obvious trend of overestimating rainfall in the TP, there appears to be underestimated during heavy rainfall events (Fig. 8). To determine the forecast capabilities of the model in the heavy rainfall periods, we focused on one heavy rainfall period of 3-5 July.

Figure 9 shows the rainfall intensities (bars) calculated for every 3 h amount of precipitation. The cumulative precipitation (curves) is defined as the precipitation accumulated for each 3 h starting at 06:00 UTC during 3–6 July. From the perspective of observations, this rainfall event can be divided into three periods, of which the 3 July is ahead of the heavy rainfall with less than 0.45 mm per 3 h, followed by the rainfall around 03:00 UTC on 4 July to 03:00 UTC on 5 July, with the first peak at 21:00 UTC on 4 July of more than 0.65 mm per 3 h. The third phase started at 03:00 UTC on 5 July and ended at 00:00 UTC on 6 July with a second rainfall pulse around 21:00 UTC on 5 July exceeding 0.60 mm per 3 h and then weakening. It is evident that this rainfall event had a significant diurnal harmonic and the maximum precipitation always occurred at 18:00–21:00 UTC (00:00–03:00 LST). This diurnal variation was remarkable, especially when the heavy rainfall occurred, which was equivalent to evening local solar time (LST). However, the simulated maximum always occurred at 06:00–09:00 UTC (12:00–15:00 LST), earlier than the observations, and can probably be attributed to the limit of complicated topography. In this case, simulated rainfall intensity was much lower than the observations during 09:00 UTC on 4 July to 00:00 UTC on 5 July and 12:00 UTC on 5 July to 21:00 UTC on 5 July when the rainfall occurred. That is, the model cannot promptly quantitatively predict the sudden occurrence of this event. Moreover, the cumulative curves of the model show an overestimation on 3 and 5 July compared with observations; in particular, the cumulative curves of the CTRL are far away from the measured values due to an inaccurate initial field. It can be concluded that the DA experiments data are closer to the observations during the heavy rainfall period compared with the CTRL experiment.

4.3 Impact of DA on circulation and water vapor supply

According to the above-mentioned analysis, it is evident that DA improves forecasts during the heavy rainfall period, but the results are not the same when different data sets are injected. As is well known, adequate water vapor transport is one of the preconditions for precipitation formation. In this section, we discuss the water vapor supply in the 3–5 July case study, with the aim of determining the reason for the different influences exerted by different experimental schemes. Figure 10 shows the F24H forecasts of precipitation quantity (shadings) and water vapor flux (vectors) during 3–5 July. Zonal component of wind velocity (u), meridional component of wind velocity (v), specific humidity (q), and covariance, which are needed for flux computations, are provided at eight standard pressure levels (1000, 925, 850, 700, 600, 500, 400, and 300 hPa). The equation of unit side length, vertically integrated between the surface level and the top of the atmosphere and averaged in time atmospheric water vapor flux (unit: $kg*m^{-1}*s^{-1}$) can be written as:

$$\vec{Q} = Q_u\vec{i} + Q_v\vec{j} \qquad (11)$$

The zonal and meridional component of vapor flux is described by:

$$Q_u = \frac{1}{g}\int_p^{p_s} qudp \qquad (12),$$

and

$$Q_v = \frac{1}{g}\int_p^{p_s} qvdp \qquad (13).$$

Where ps is the surface pressure and p is the pressure at the "top" of the atmosphere, g is the gravitational constant ($9.8\ m*s^{-2}$).

The water vapor flux divergence (D, unit: $kg•m^{-2}•s^{-1}$) is given by:

$$D = \frac{\partial Q_u}{a\cos\varphi\,\partial\sigma} + \frac{\partial Q_v}{a\,\partial\varphi} \qquad (14)$$

where a is the radius of the model earth taken as 6371.2 km, φ is latitude in radians, and σ is longitude in radians.

According to observations, warm and humid water vapor is transferred from the Bay of Bengal eastward by the southwest monsoon. The TP blocks the westward transport of humid and warm air, and this rainfall event start developing in the southeast of the TP on 3 July and then the rainbelt runs southeast to southwest and develops along the Himalayas on 4–5 July. Comparing the observations (Fig. 10a–c) with model results (Fig. 10d–f), the simulated precipitation is considerably larger than the observed on 3 July before the heavy rainfall occurs, but as time goes on this condition reverses. For the difference value distribution (Fig. 10g–i) of the CTRL minus observations, the main water vapor flux divergence differences (shadings) are negative in the rainy region on 3 July, which indicates that the water vapor convergence is stronger than observed, inducing the overestimation. However, when the rainfall event occurs on 4–5 July, this condition is opposite. The water vapor differences (vectors) also suggest that the observed water vapor conveyance from the southeastern of the TP is larger than the model simulation, which induces inaccuracies in the forecast of the heavy rain. Therefore, analysis of moisture is useful for improving the heavy rainfall forecasting skill.

To further discuss the effect of DA on this rainfall event, the differences between the simulated F24H precipitation and the observed distribution and the FSS skill scores (Fig. 11) were considered. From the spatial distribution, all the experiments (Fig. 11a, d, g, j) overestimated the precipitation quantity, especially the CTRL, before the heavy rainfall and the FSS skill scores all ranged from 0.46 to 0.49 with little differences (bottom left in Fig. 11m). When the heavy rainfall event occurred on 4 July, the observed rainbelt moved southwest (Fig. 11b, e, h, k), while the simulated rainbelt was motionless, leading to an underestimation in the southwest. The FSS scores for ATMS, CONV and CTRL ranged from 0.42 to 0.48 (middle in Fig. 11m), but CRIS only scored 0.36. As the water vapor conveyance directly contributes to the westward movement of the rainbelt and the intensity of this precipitation event on 5 July, the precipitation experiments all underestimated the amount of precipitation, and CRIS performed particularly badly (Fig. 10c, f, i). However, ATMS had a substantially high FSS scores (0.47) (right in Fig. 11m), followed by CRIS (0.45) and CONV (0.43) while CTRL only scored 0.35. This result indicates that DA can indeed improve the heavy rainfall forecast. From the above analysis of Figure 9 and 11, it is clear that before the heavy rainfall, DA can improve the simulation of precipitation spatially. As time passes and the heavy rainfall develops, DA, especially the ATMS assimilation, can enhance model prediction abilities both spatially and temporally in comparison with the CTRL experiment.

5. Summary and discussion

In this study, we used diagnostic methods to analyze the impact of DA on the monthly precipitation distribution over the TP and then focused on one heavy rainfall case study that occurred from 3 to 5 July 2015. The DA and NWP were performed for July 2015 to make the weather forecasts. The spatial distribution of monthly mean precipitation showed an evident rain shadow effect along the Himalayas and that the precipitation decreased northward in the TP. However, the simulated precipitation belt was shifted northward compared with the observed rainbelt and showed an orographic bias described as an overestimation in the upwind of the mountains and an underestimation in the south of the rainbelt. Assimilation of satellite radiance also can not calibrate the rain shadow effect and all experiments showed consistently gross overestimation patterns. Furthermore, it seems that the rain shadow mainly influences prediction of the quantity of precipitation, but the main rainfall pattern can be well predicted. Comparisons indicate that the WRF-ARW model has promising potential, in that the false alarms are primarily predicted in the east of the TP in contrast to the misses in the west. The DA validation statistics also suggest that DA has a positive effect on monthly mean precipitation prediction in the TP compared with the CTRL to varying degrees. For the time series of monthly precipitation, F24H and L24H precipitation chiefly overestimate the amount of precipitation, which is in agreement with previous studies, but the amount of 24 h precipitation in the three heavy rainfall periods of 3–5, 13–16, and 22–25 July is underestimated.

To further study the underestimations in the heavy rainfall events and the performance of the WRF-ARW model and GSI DA impact, we selected a case study from 3 to 5 July. It is evident that this rainfall event had a significant diurnal harmonic and the maximum precipitation always occurred at 18:00–21:00 UTC (00:00–03:00 LST). This diurnal variation was remarkable, especially when the heavy rainfall occurred. Although the model can not promptly quantitatively predict the sudden occurrence of this rainfall event, the DA, especially the ATMS simulation are closer to the observations for the heavy rainfall event compared with CTRL experiments. Overall, before the heavy rainfall, DA improved the precipitation prediction spatially. As time passed and the rainbelt moved and rainfall developed, DA enhanced the model prediction abilities both spatially and temporally. It should be mentioned that the high altitude and complex topography of the TP and its blocking effect on moisture transfer coming from Indian Ocean by the southwest monsoon obviously influences the rainfall forecast. As precipitation biases indicate some extent of spatial coherence and temporal recurrence, it is possible to provide an adapted correction method to enhance the model precipitation prediction capabilities.

It is conspicuous that the ATMS showed better performance than CTRL, CONV, and CRIS in the case study. Past studies have indicated that the effect of assimilation of both observations and satellite products is better than assimilation of satellite data only, which may account for the ATMS performing better than CONV. ATMS also performed better than CRIS. As clouds are opaque in the infrared wave band of the spectrum and largely transparent in the microwave band, microwave instruments are thought to perform better than infrared instruments on cloudy and rainy days, which may explain the better performance of ATMS compared with CRIS.

In this study, we investigated the monthly precipitation distribution and a selected heavy rainfall case in the TP using the WRF-ARW mesoscale model and the GSI data assimilation system. Moisture and dynamic conditions were analyzed in the case study; however, thermal conditions are also one of the direct factors leading to rainfall that need to be investigated in the future.

Furthermore, although the CrIS were assimilated large amount of satellite radiance pixels, the general DA effect is relatively worse compared with the other three experiments. CrIS has 1305 spectral channels, some of which are redundant as they include many satellite radiance observations from similar altitudes and contain much repeated information, which may lead to the poor DA impact. It should take the priority to select physical sensitivity and the high vertical resolution channels. On the other hand, the high altitude and complicated dynamic, thermal conditions increase the difficulty of selecting channels. Therefore, only by carrying out further research on bias correction, quality control, and channel selection can satellite radiance data play an efficient role in TP weather forecasting.

In addition, model resolution and parameterized scheme selection are also key factors affecting forecast quality. In this study, the parameterized schemes we choose have been applied in previous studies of the TP. It would be worthwhile to make a comparative analysis of different parameterized schemes with higher model resolution in the future. Furthermore, it should be noted that due to the heavy calculation burden, this study made use of 3D-Var as the assimilation method. Other advanced assimilation techniques, such as 4D-Var, Hybrid, and EnKF, also need to be tested.

Acknowledgements

The WRF-ARW model was obtained from NCAR, the GSI data assimilation system was obtained from JCSDA, and the satellite datasets were provided by NOAA/NESDIS/STAR. The authors are very grateful to these agencies for the model and providing data. This work was jointly supported by the Special Fund for Public Welfare of China Meteorological Administration (GYHY201406024) and the National Natural Science Foundation of China (91437104, 41130960). The corresponding author was supported by the National Innovation Project for Meteorological Science and Technology: Quality Control, Fusion, and Reanalysis of

Meteorological Observations and the Guangdong Ocean University Research Funding of Air–Sea Interaction and Data Assimilation (300702/E16188). The first author was a visiting scholar at GMU/AOES during this study and acknowledges helpful discussions with fellow members of GMU/AOES.

Reference

Bormann, N., A. Fouilloux, and W. Bell: Evaluation and assimilation of ATMS data in the ECMWF system, *Journal of Geophysical Research: Atmospheres*, *118*(23), 2013

Chambon, P., S. Q. Zhang, A. Y. Hou, M. Zupanski, and S. Cheung: Assessing the impact of pre-GPM microwave precipitation observations in the Goddard WRF ensemble data assimilation system, *Quarterly Journal of the Royal Meteorological Society*, *140*(681), 1219-1235, 2014

Chen, Y., L. Ji, and R. Shen: The numerical experiments on dynamic forcing by the Tibetan Plateau for various zonal flows, *Advances in Atmospheric Sciences*, *2*(2), 189-199, 1985

Derber, J. C., and W. S. Wu: The use of TOVS cloud-cleared radiances in the NCEP SSI analysis system, *Monthly Weather Review*, *126*(8), 2287-2299, 1998

Dong, P., Liu, J., Liu, G., & Huang, J.: Study on the assimilation of ATMS satellite data and comparison with AMSUA/MHS, *Journal of Tropical Meteorology,* 30(4), 623-632, 2014

Eyre, J. R.: *A bias correction scheme for simulated TOVS brightness temperatures*, European Centre for Medium-Range Weather Forecasts, 1992

Gao, Y. C., and Liu, M. F. Evaluation of high-resolution satellite precipitation products using rain gauge observations over the tibetan plateau. *Hydrology & Earth System Sciences Discussions*, 2013, 9(8), 9503-9532.

Gao, Y., J. Xu, and D. Chen: Evaluation of WRF Mesoscale Climate Simulations over the Tibetan Plateau during 1979–2011, Journal of Climate, 28(7), 2823-2841, 2015

Gauthier, P., M. Tanguay, S. Laroche, S. Pellerin, and J. Morneau: Extension of 3DVAR to

4DVAR: Implementation of 4DVAR at the Meteorological Service of Canada, Mon. Wea. Rev., 135, 2339–2354, 2007

Guo, J., Zhai, P., Wu, L., Cribb, M., Li, Z., Ma, Z., & Zhang, J.: Diurnal variation and the influential factors of precipitation from surface and satellite measurements in Tibet, *International Journal of Climatology*, *34*(9), 2940-2956, 2014

Han, Y., P. Delst, Q. Liu, F. Weng, B. Yan, R. Treadon, and J. Derber: JCSDA Community Radiative Transfer Model-Version 1 (CRTM-V1), *NOAA Tec,* (122), 40, 2006

He, Y., K. Yang, T. Yao, and J. He: Numerical Simulation of a Heavy Precipitation in Qinghai-Xizang Plateau Based on WRF Model, *Plateau Meteorology (in Chinese)*, 31(5), 1185-1186, 2012

Developmental Testbed Center, 2016 : Gridpoint Statistical Interpolation Advanced User's Guide Version 3.5. Available at http://www.dtcenter.org/com-GSI/users.v3.5/docs/index.php, 119 pp.

Hubbard, K. G., and J. You: Sensitivity analysis of quality assurance using the spatial regression approach-A case study of the maximum/minimum air temperature, *Journal of Atmospheric and Oceanic Technology*, *22*(10), 1520-1530, 2005

Kazumori, M.: Satellite radiance assimilation in the JMA operational mesoscale 4DVAR system, *Monthly Weather Review*, *142*(3), 1361-1381, 2014.

Liu, Q. and F. Weng: Detecting the warm core of a hurricane from the Special Sensor Microwave Imager Sounder, Geophys. Res. Lett., 33, 2006

Liu, Z., C. S. Schwartz, C. Snyder, and S. Y. Ha: Impact of assimilating AMSU-A radiances on forecasts of 2008 Atlantic tropical cyclones initialized with a limited-area ensemble Kalman filter, *Monthly Weather Review*, *140*(12), 4017-4034, 2012

Liu, J., M. Bray, and D. Han: A study on WRF radar data assimilation for hydrological rainfall prediction, *Hydrology and Earth System Sciences*, *17*(8), 3095-3110, 2013

Marteau, R., Y. Richard, B. Pohl, C. C. Smith, and T. Castel: High-resolution rainfall variability simulated by the WRF RCM: application to eastern France, *Climate Dynamics*, *44*(3-4), 1093-1107, 2015

Massacand, A. C., H. Wernli, and H. C. Davies: Heavy precipitation on the Alpine southside: An upper-level precursor, *Geophysical Research Letters*, *25*(9), 1435-1438, 1998

Maussion, F., D. Scherer, R. Finkelnburg, and J. Richters: WRF simulation of a Precipitation event over the Tibetan Plateau, China-an assessment using remote sensing and ground observations, 2011

Newman, K. M., C. S. Schwartz, Z. Liu, H. Shao, and X.-Y. Huang: Evaluating Forecast Impact of Assimilating Microwave Humidity Sounder (MHS) Radiances with a Regional Ensemble Kalman Filter Data Assimilation System, *Weather and Forecasting*, *30*(4), 964-983, 2015

Pan, Y., Y. Shen, Q.-Q. Yu, and P. Zhao: Merged analyses of gauge-satellite hourly precipitation over China based on OI technique (in Chinese with English abstract), Acta Meteor. Sin, 70, 1381-1389, 2012

Purser, R. J., Wu, W. S., Parrish, D. F., and Roberts, N. M: Numerical aspects of the application of recursive filters to variational statistical analysis. Part I: Spatially homogeneous and isotropic Gaussian covariances. *Monthly Weather Review*, 131(8), 1524-1535, 2003a

Purser, R. J., Wu, W. S., Parrish, D. F., and Roberts, N. M: Numerical aspects of the application of recursive filters to variational statistical analysis. Part II: Spatially inhomogeneous and anisotropic general covariances. *Monthly Weather Review*, 131(8), 1536-1548, 2003b

Roberts, N. M., and H. W. Lean: Scale-selective verification of rainfall accumulations from high-resolution forecasts of convective events, Mon. Wea. Rev., 136, 78–97, 2008

Saunders, R., M. Matricardi, and P. Brunel: An improved fast radiative transfer model for assimilation of satellite radiance observations, *Quarterly Journal of the Royal Meteorological Society*, *125*(556), 1407-1425, 1999

Schwartz, C. S., Z. Liu, Y. Chen, X. Y. Huang: Impact of assimilating microwave radiances with a limited-area ensemble data assimilation system on forecasts of Typhoon Morakot, *Weather and Forecasting*, *27*(2), 424-437, 2012.

Shen, Y., P. Zhao, Y. Pan, and J. Yu: A high spatiotemporal gauge-satellite merged precipitation analysis over China, *Journal of Geophysical Research: Atmospheres*, *119*(6), 3063-3075, 2014.

Tong, K., Su, F., Yang, D., and Hao, Z. Evaluation of satellite precipitation retrievals and their potential utilities in hydrologic modeling over the tibetan plateau. *Journal of Hydrology*, 2014, 519, 423–437.

Wang, C. H., S. W. Zhou, X. P. Tang, and P. Wu: Temporal and spatial distribution of heavy precipitation over Tibetan Plateau in recent 48 years, *Scientia Geographica Sinica*, *31*(4), 470-477, 2011.

Wei, Z., R. H. Huang, W. J. Dong: Interannual and interdecadal variations of air temperature and precipitation over the Tibetan Plateau, *Chinese Journal of Atmospheric Sciences*, 27(2), 157-170, 2003

Weng, F.: Advances in radiative transfer modeling in support of satellite data assimilation. *Hyperspectral Imaging and Sensing of the Environment* (p. HWD1), Optical Society of America, 2009

Wu, W., R. Purser, and D. Parrish: Three-Dimensional Variational Analysis with Spatially Inhomogeneous Covariances. *Mon. Wea. Rev*., 130, 2905–2916, 2002

Xie, P., and A. Y. Xiong: A conceptual model for constructing high-resolution gauge-satellite merged precipitation analyses, *Journal of Geophysical Research: Atmospheres*, 116(D21) , 2011

Xu, J., S. Rugg, L. Byerle, and Z. Liu: Weather forecasts by the WRF-ARW model with the GSI data assimilation system in the complex terrain areas of southwest Asia, *Weather and Forecasting*, *24*(4), 987-1008, 2009

Xu, J., B. Zhang, M. Wang, and H. Wang: Diurnal variation of summer precipitation over the Tibetan Plateau: a cloud-resolving simulation, *Annales Geophysicae,* 30(11), 1575-1586, 2012

Xu, J. and A. Powell: Dynamical downscaling precipitation over the Southwest Asian: impacts of radiance data assimilation on the hindcasts of the WRF-ARW model, Atmos. Res., 111, 90–103, 2012

Ye, D. Z., and Y. X. Gao: Tibetan Plateau Meteorology. *Science, Beijing*, 89-101, 1979

Zapotocny, T. H., J. A. Jung, J. F. Le Marshall, and R. E. Treadon: A two-season impact study of four satellite data types and rawinsonde data in the NCEP Global Data Assimilation System, *Weather and Forecasting*, *23*(1), 80-100, 2008

Zhang, X., X, B., & X, K.: Observed diurnal cycle of summer precipitation over South Asia and East Asia based on CMORPH and TRMM satellite data, *Atmospheric and Oceanic Science Letters*, *8*(4), 201-207, 2015

Zhao, X. Y., Y. R. Wang, Q. Zhang, and L. Luo: Climatic characteristics of heavy precipitation events during summer half year over the Eastern Tibetan Plateau in recent 50 years, *Arid Land Geography*, *4*, 004, 2015.

Zhu, F., G. Xu, and L. Li: An assessment of the impact on precipitation prediction in the middle and lower reaches of the Yangtze River made by assimilating GPSPW data in the Tibetan Plateau, *Chinese Journal of Atmospheric Sciences (in Chinese)*, 38 (1): 171–189, 2014

Zhu, Y., J. Derber, A.Collard, D. Dee, R. Treadon, G. Gayno, J. Jung: Enhanced radiance bias correction in the National Centers for Environmental Prediction's Gridpoint Statistical Interpolation data assimilation system. *Quarterly J. Royal. Meteorol. Soc.*, 140, 1479-1492, 2014.

Zou, X., Z. Qin, and F. Weng: Improved coastal precipitation forecasts with direct assimilation of

GOES-11/12 imager radiances, *Monthly Weather Review*, *139*(12), 3711-3729, 2011

Zou, X., Z. Qin, and F. Weng: Improved quantitative precipitation forecasts by MHS radiance data assimilation with a newly added cloud detection algorithm, *Monthly Weather Review*, *141*(9), 3203-3221, 2013.

Table 1. The channels for ATMS and CrIS data that have been selected for the data assimilation procedure

Sensor	Channels
ATMS	1-14, 16-22
CrIS	37, 49, 51, 53, 59, 61, 63, 65, 67, 69, 71, 73, 75, 77, 79, 80, 81, 83, 85, 87, 89, 93, 95, 96, 99, 101, 102, 104, 106, 107, 116, 120,123, 124,,125, 126, 130, 132, 133, 136, 137, 138, 142,143, 144, 145, 147, 148, 150, 151, 153, 154, 155, 157-168, 170, 171, 173, 175, 198, 211, 224, 279, 342, 392, 404, 427, 464, 482, 501, 529

Table 2. Rain contingency table used in the verification studies. As a threshold, 6 mm day^{-1} is chose to separate rain from no-rain events

Forecast	Observed	
	Yes	No
Yes	Hits	False alarms
No	Misses	Correct rejections

Figure captions

Figure 1. (a) Simulation domains and topography. Resolutions are at 12 km and 4 km for the outer (coarse grid, D01) and inner (nested grid, D02) boxes, respectively. The shading indicates the terrain elevation (unit: m). (b)–(d) Distribution of (b) conventional data observations, (c) scan coverage of ATMS data after data assimilation, and (d) scan coverage of CrIS data after data assimilation at 06:00 UTC on 1 July 2015.

Figure 2. Blue bars indicate the total amount of radiance read in the DA system. Red bars present the number of kept radiance after first step of quality control. The used percentage after final quality control is shown as black curves. The right y-axis indicates the ratio of used amount to read amount. Top panel is for ATMS (a) and bottom is for CrIS data (b).

Figure 3. Top panel shows the schematic of data assimilation configuration with 3D-Var. Bottom panel presents the experiments design. CTRL: control experiment without data assimilation that the initial time is 00:00 UTC from 1 to 31 July; CONV: data assimilation with conventional data only; ATMS: data assimilation with conventional and ATMS data; CRIS: data assimilation with conventional and CrIS data. CONV, ATMS and CRIS experiments all start at 06:00 UTC from 1 to 31 July.

Figure 4. Daily precipitation averaged (unit: mm) for the month of July 2015. (a), (b) are F24H forecast and (c), (d) are L24H forecast. Black contours are altitude (unit: m).

Figure 5. Difference value distribution of monthly mean precipitation (unit: mm) during July for

data assimilation minus observation experiments. (a), (e) CTRL minus OBS; (b), (f) CONV minus OBS; (c), (g) ATMS minus OBS (d),(h) CRIS minus OBS for (a)–(d) F24Hforecast and (e)–(h) L24Hforecast. Black contours are altitude (unit: m).

Figure 6. Spatial patterns of (a)–(d) the contingency table and (e)–(h) the scatter plots (monthly mean F24 h rainfall over 6 mm threshold is defined as an "event"). The solid grey line indicate the regression line of A. Black contours are altitude (unit: m).

Figure 7. Monthly and domain average validation statistics for F24H forecast (a–f) and L24H forecast (g–l). (a) and (g) are Bias Score; (b) and (h) are Fraction skill Score; (c) and (i) are Equitable Threat Score; (d) and (j) are Probability of False Detection; (e) and (k) are Probability of Detection; (f) and (l) are False Alarm ratio.

Figure 8. Time series of daily precipitation distribution for F24H forecast (a) and L24H forecast (b). The black, grey, blue, red and green lines indicate observation, CTRL, CONV, ATMS and CRIS, respectively. The unit is mm. The grey shadings indicate the underestimated events.

Figure 9. Rainfall intensities (bars) calculated for every 3 h amount of precipitation. The cumulative precipitation (curves) is defined as the precipitation accumulated for each 3 h starting at 06:00 UTC during 3–5 July. The unit is mm.

Figure 10. (a)–(f) 24 h forecasts of precipitation quantity (shadings) and water vapor flux (vectors) during 3–5 July for (a)–(c) OBS and (d)–(f) CTRL. (g)–(i) Differences in water vapor flux (vectors) and water vapor divergence (shadings) between CTRL and

OBS. The unit of precipitation is mm. The units for water vapor flux and divergence is kg/(m*s) and kg/(m^2*s), respectively.

Figure 11. (a)–(l) are differences between the simulated F24H precipitation and the observed distribution and (m) is the FSS skill scores with 8 mm threshold during 3–5 July. The unit of differences is mm.

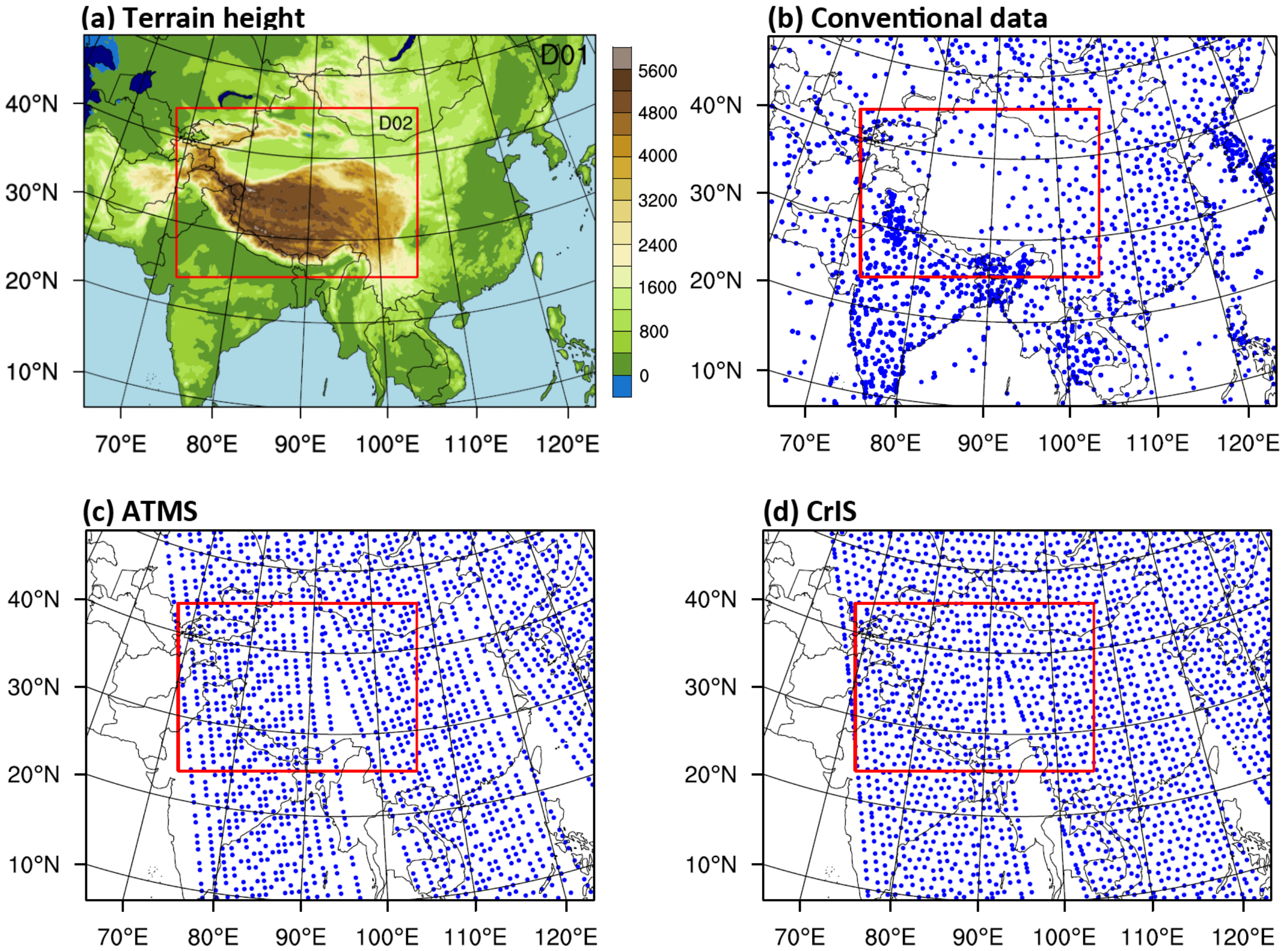

Figure 1. (a) Simulation domains and topography. Resolutions are at 12 km and 4 km for the outer (coarse grid, D01) and inner (nested grid, D02) boxes, respectively. The shading indicates the terrain elevation (unit: m). (b)–(d) Distribution of (b) conventional data observations, (c) scan coverage of ATMS data after data assimilation, and (d) scan coverage of CrIS data after dta assimilation at 06:00 UTC on 1 July 2015.

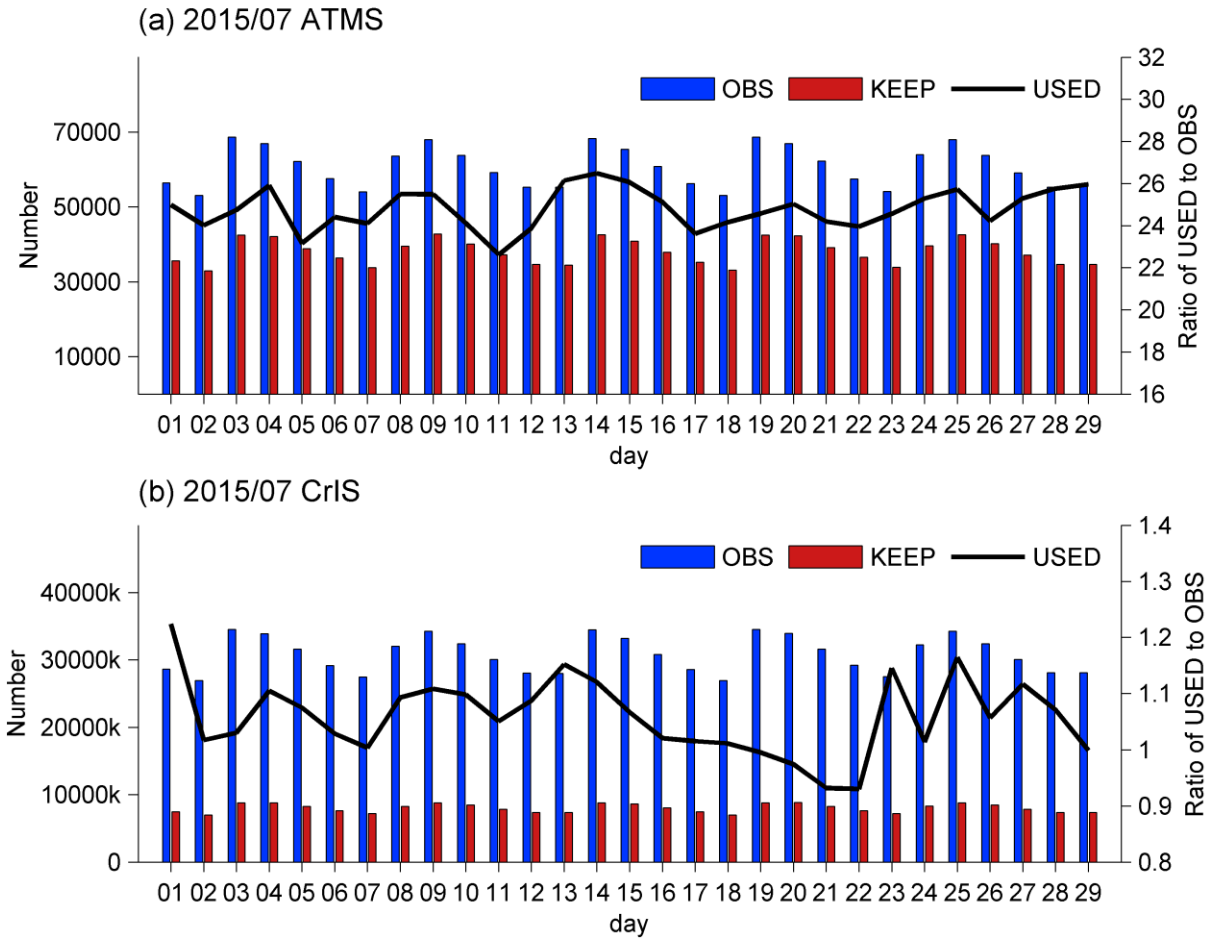

Figure 2. Blue bars indicate the total amount of radiance read in the DA system. Red bars present the number of kept radiance after first step of quality control. The used percentage after final quality control is shown as black curves. The right y-axis indicates the ratio of used amount to read amount. Top panel is for ATMS (a) and bottom is for CrIS data (b).

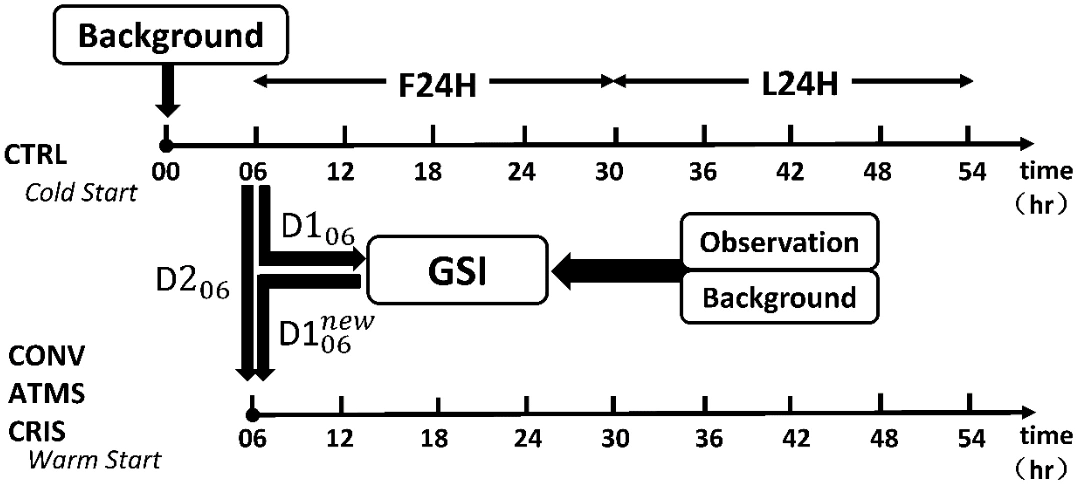

EXP	Description	Initial time
CTRL	No assimilation	00:00 UTC from 1 Jul to 31 Jul
CONV	Conventional data only	06:00 UTC from 1 Jul to 31 Jul
ATMS	Conventional + ATMS data	06:00 UTC from 1 Jul to 31 Jul
CRIS	Conventional + CrIS data	06:00 UTC from 1 Jul to 31 Jul

Figure 3. Top panel shows the schematic of data assimilation configuration with 3D-Var. Bottom panel presents the experiments design. CTRL: control experiment without data assimilation that the initial time is 00:00 UTC from 1 to 31 July; CONV: data assimilation with conventional data only; ATMS: data assimilation with conventional and ATMS data; CRIS: data assimilation with conventional and CrIS data. CONV, ATMS and CRIS experiments all start at 06:00 UTC from 1 to 31 July.

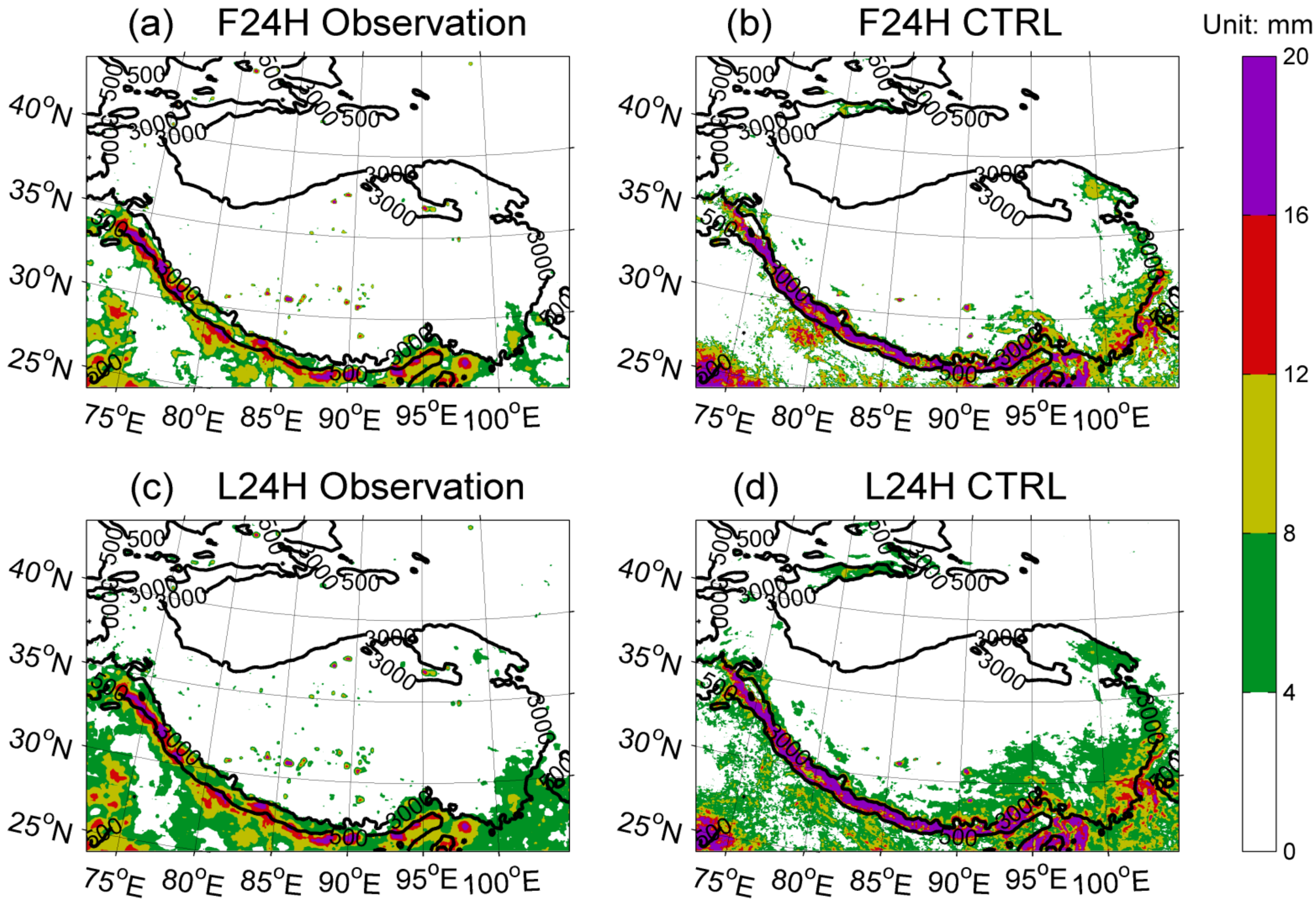

Figure 4. Daily precipitation averaged (unit: mm) for the month of July 2015. (a), (b) are F24H forecast and (c), (d) are L24H forecast. Black contours are altitude (unit: m).

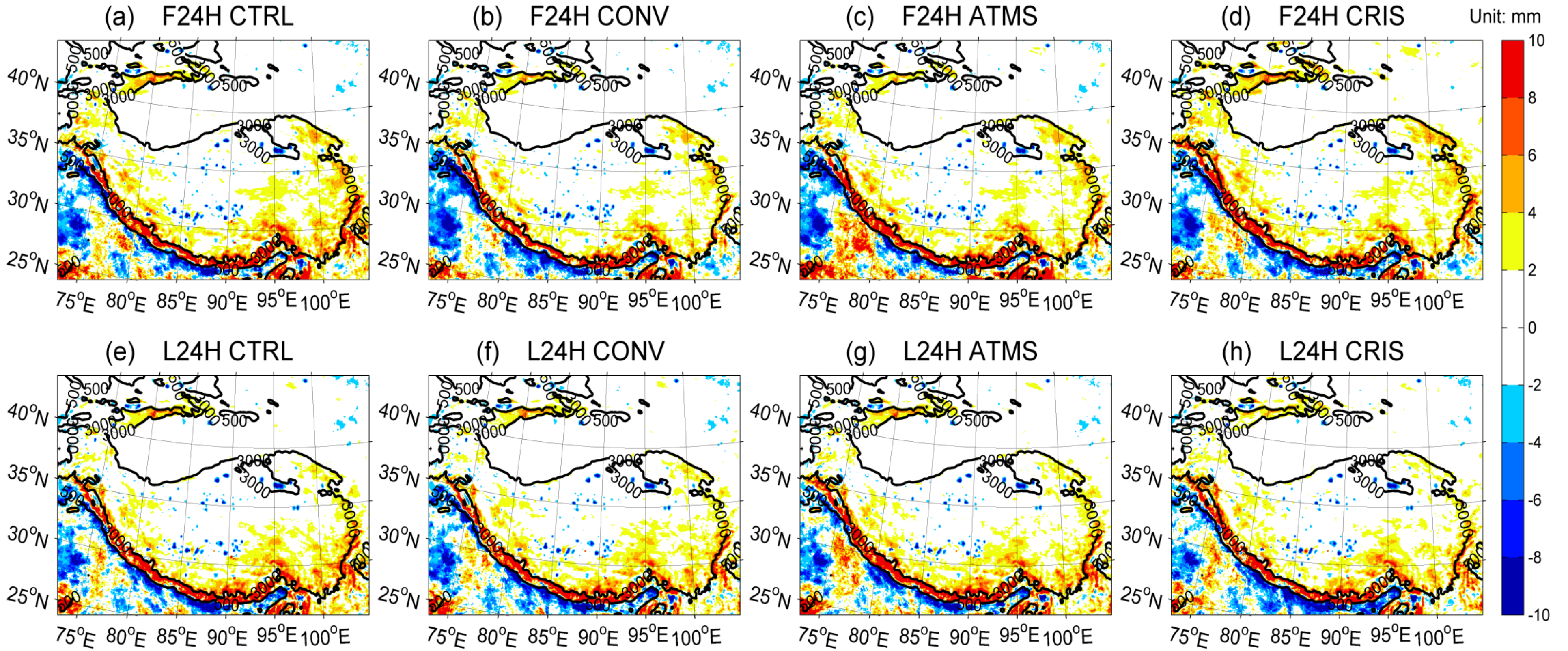

Figure 5. Difference value distribution of monthly mean precipitation (unit: mm) during July for data assimilation minus observation experiments. (a), (e) CTRL minus OBS; (b), (f) CONV minus OBS; (c), (g) ATMS minus OBS (d),(h) CRIS minus OBS for (a)–(d) F24Hforecast and (e)–(h) L24Hforecast. Black contours are altitude (unit: m).

738

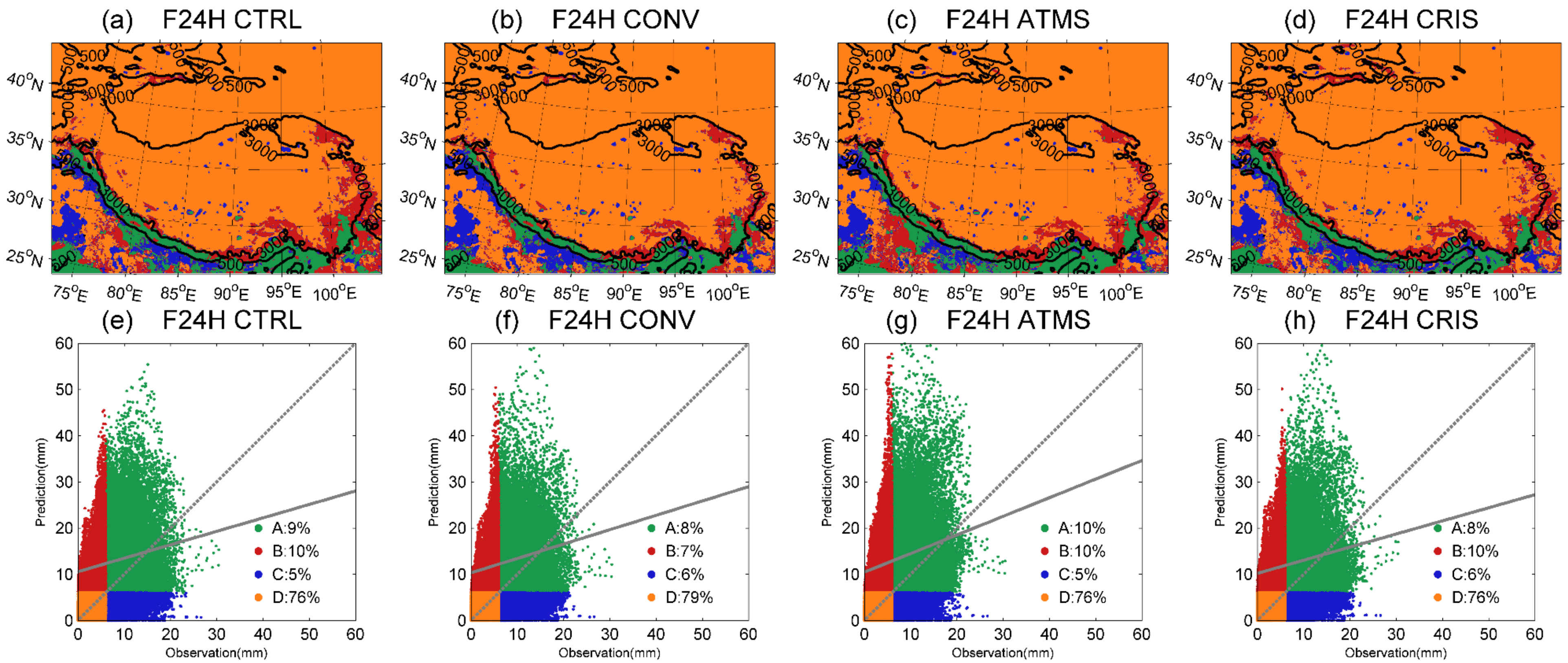

Figure 6. Spatial patterns of (a)–(d) the contingency table and (e)–(h) the scatter plots (monthly mean 24 h rainfall over 6 mm threshold is defined as an "event"). A, B, C and D indicate the Hits, False alarms, Misses and Correct rejections in Table 2, respectively. The solid grey lines indicate the regression line of A. Black contours are altitude (unit: m).

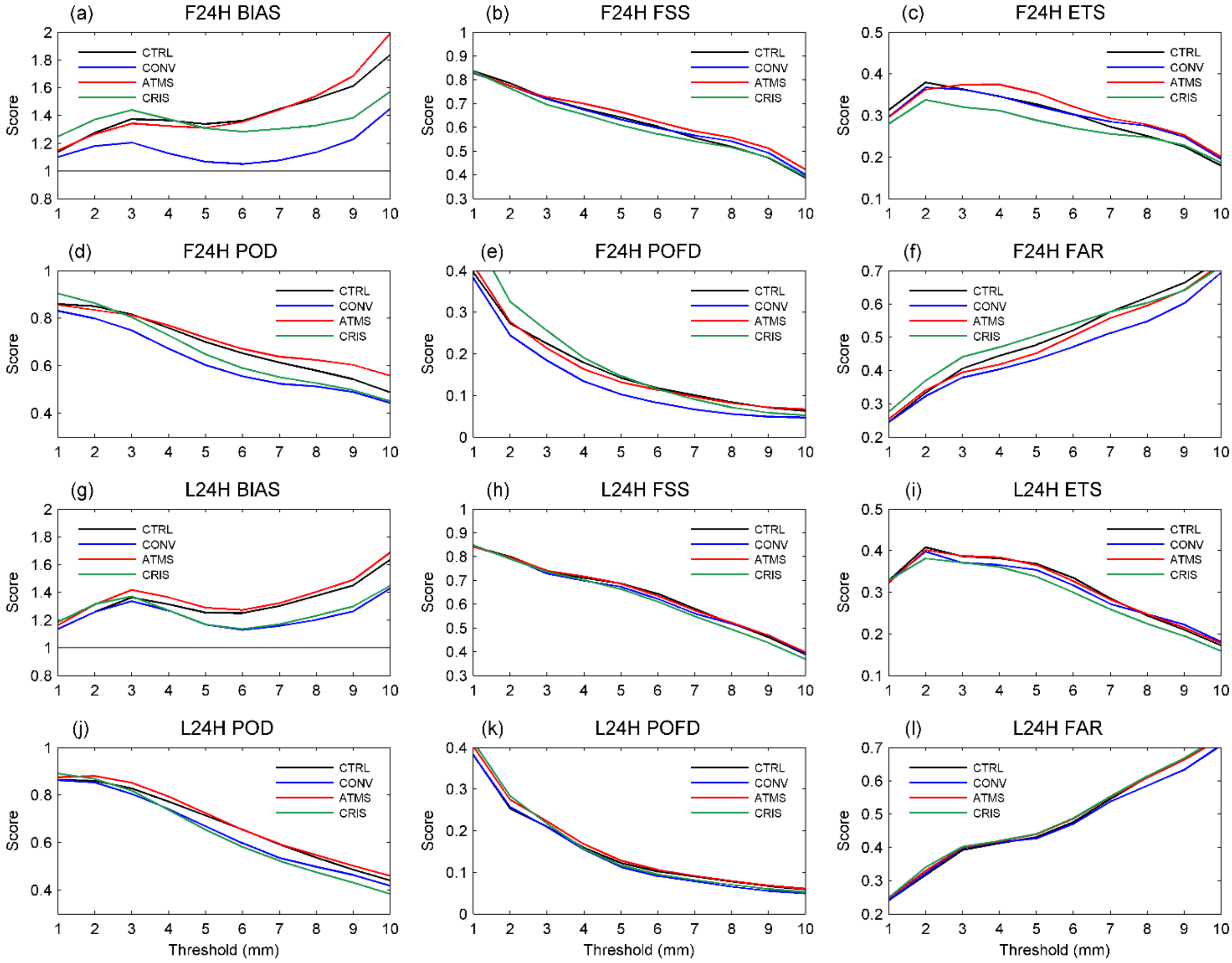

Figure 7. Monthly and domain average validation statistics for F24H forecast (a–f) and L24H forecast (g–l). (a) and (g) are Bias Score; (b) and (h) are Fraction skill Score; (c) and (i) are Equitable Threat Score; (d) and (j) are Probability of False Detection; (e) and (k) are Probability of Detection; (f) and (l) are False Alarm ratio.

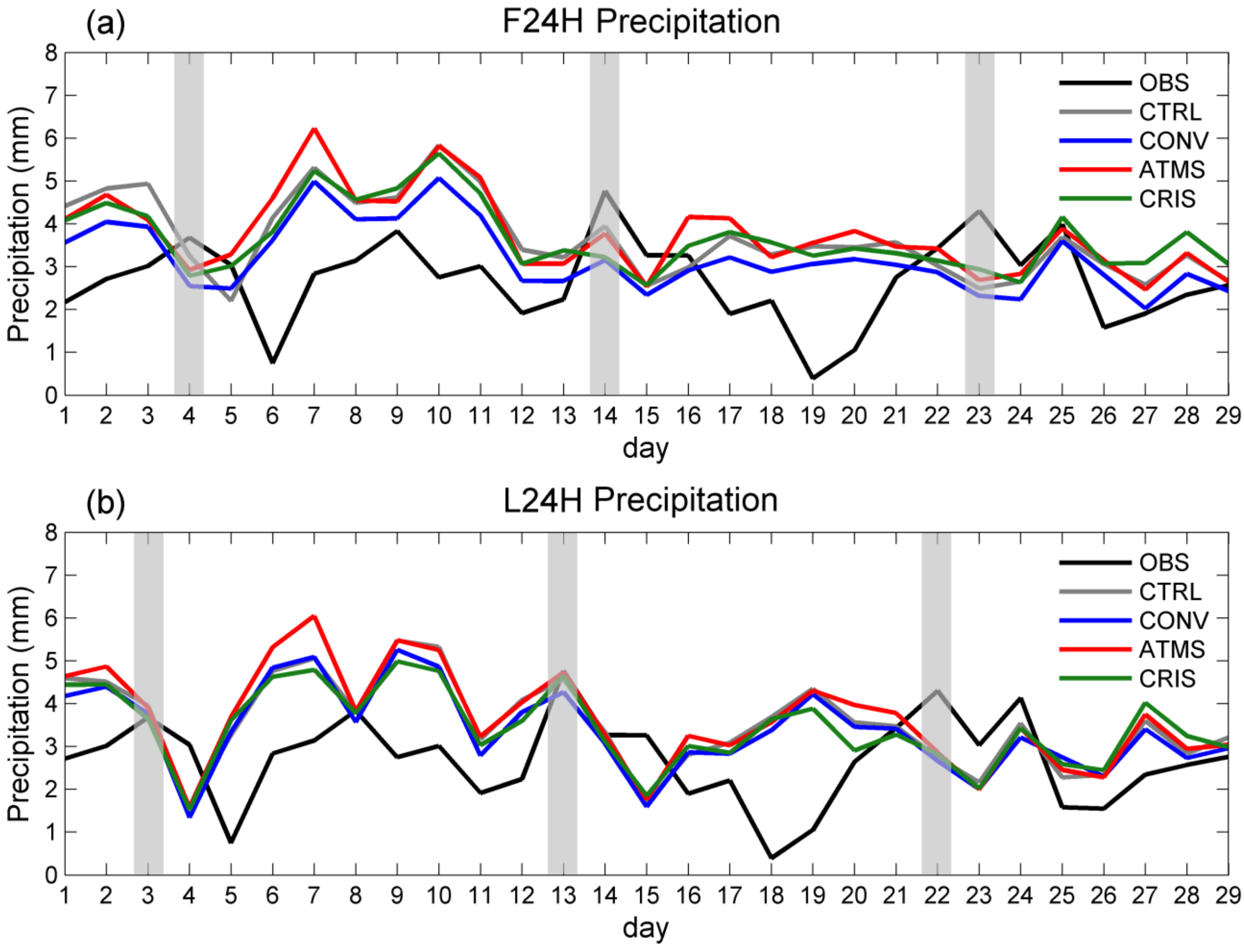

Figure 8. Time series of daily precipitation distribution for F24H forecast (a) and L24H forecast (b). The black, grey, blue, red and green lines indicate observation, CTRL, CONV, ATMS and CRIS, respectively. The unit is mm. The grey shadings indicate the underestimated events.

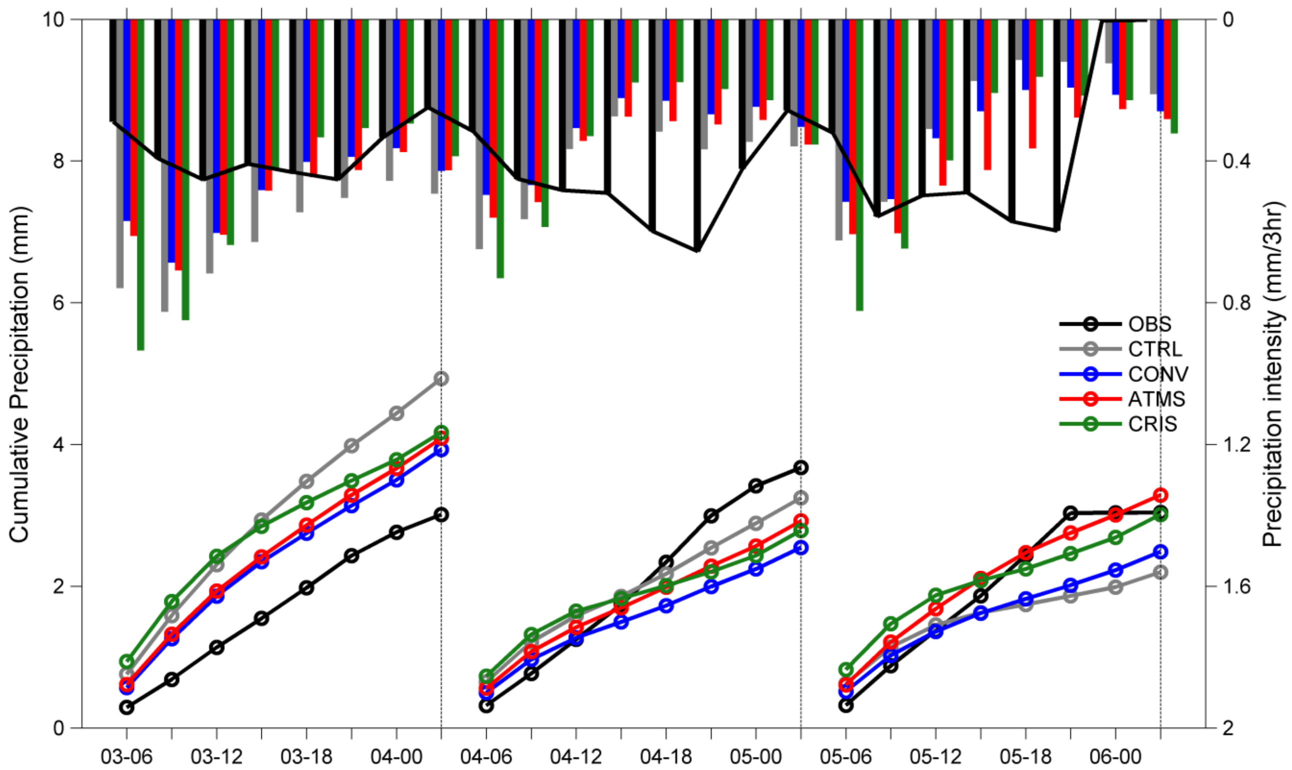

Figure 9. Rainfall intensities (bars) calculated for every 3 h amount of precipitation. The cumulative precipitation (curves) is defined as the precipitation accumulated for each 3 h starting at 06:00 UTC during 3–5 July. The unit is mm.

757

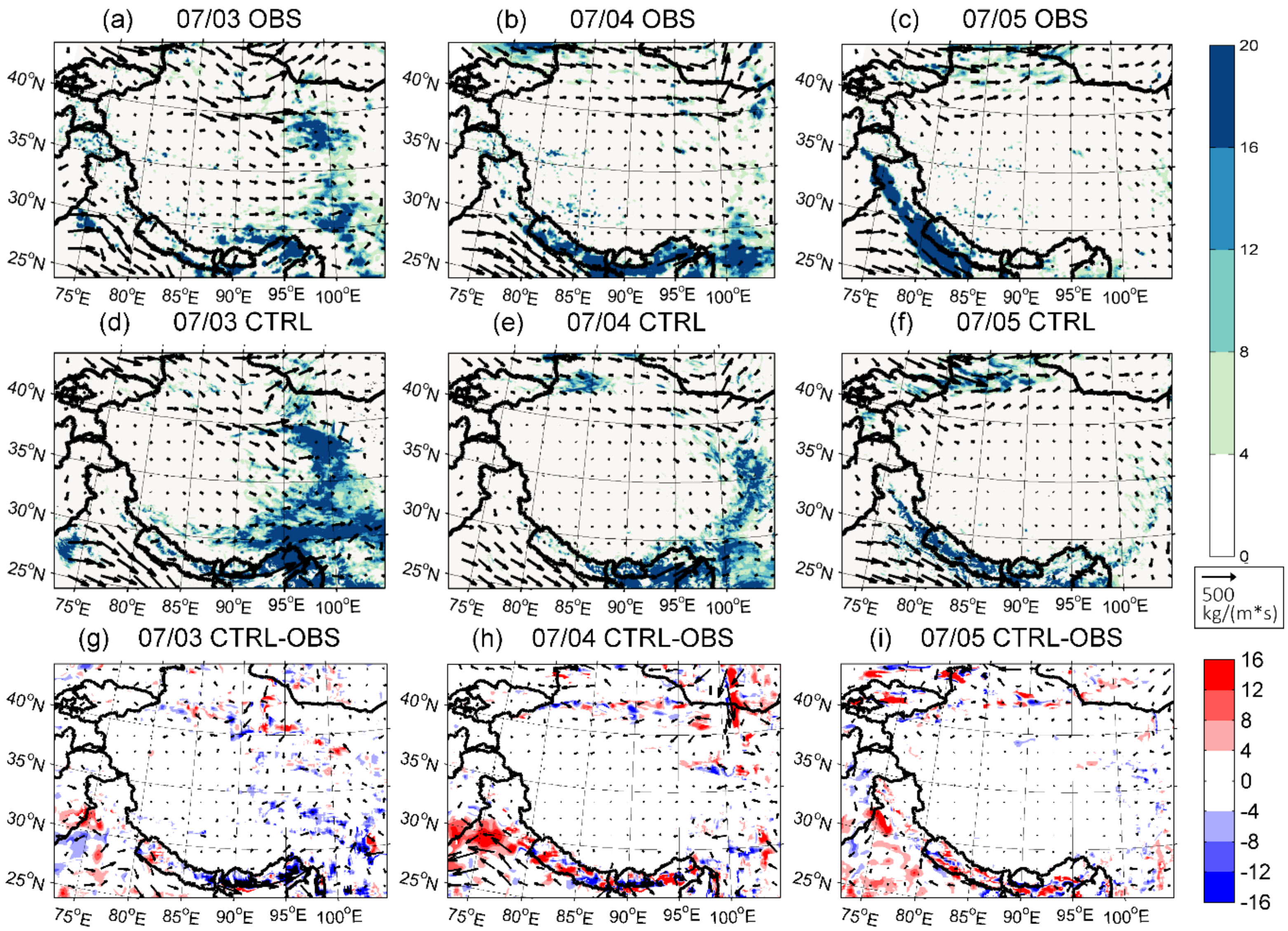
(a) 07/03 OBS
(b) 07/04 OBS
(c) 07/05 OBS
(d) 07/03 CTRL
(e) 07/04 CTRL
(f) 07/05 CTRL
(g) 07/03 CTRL-OBS
(h) 07/04 CTRL-OBS
(i) 07/05 CTRL-OBS
40°N
35°N
30°N
25°N
75°E
80°E
85°E
90°E
95°E
100°E
20
16
12
8
4
0
500 kg/(m*s)
16
12
8
4
0
-4
-8
-12
-16

Figure 10. (a)–(f) F24H forecasts of precipitation (shadings) and water vapor flux (vectors) during 3–5 July for (a)–(c) OBS and (d)–(f) CTRL. (g)–(i) Differences in water vapor flux (vectors) and water vapor divergence (shadings) between CTRL and OBS. The unit of precipitation is mm. The units for water vapor flux and divergence is kg/(m*s) and kg/(m^2*s), respectively.

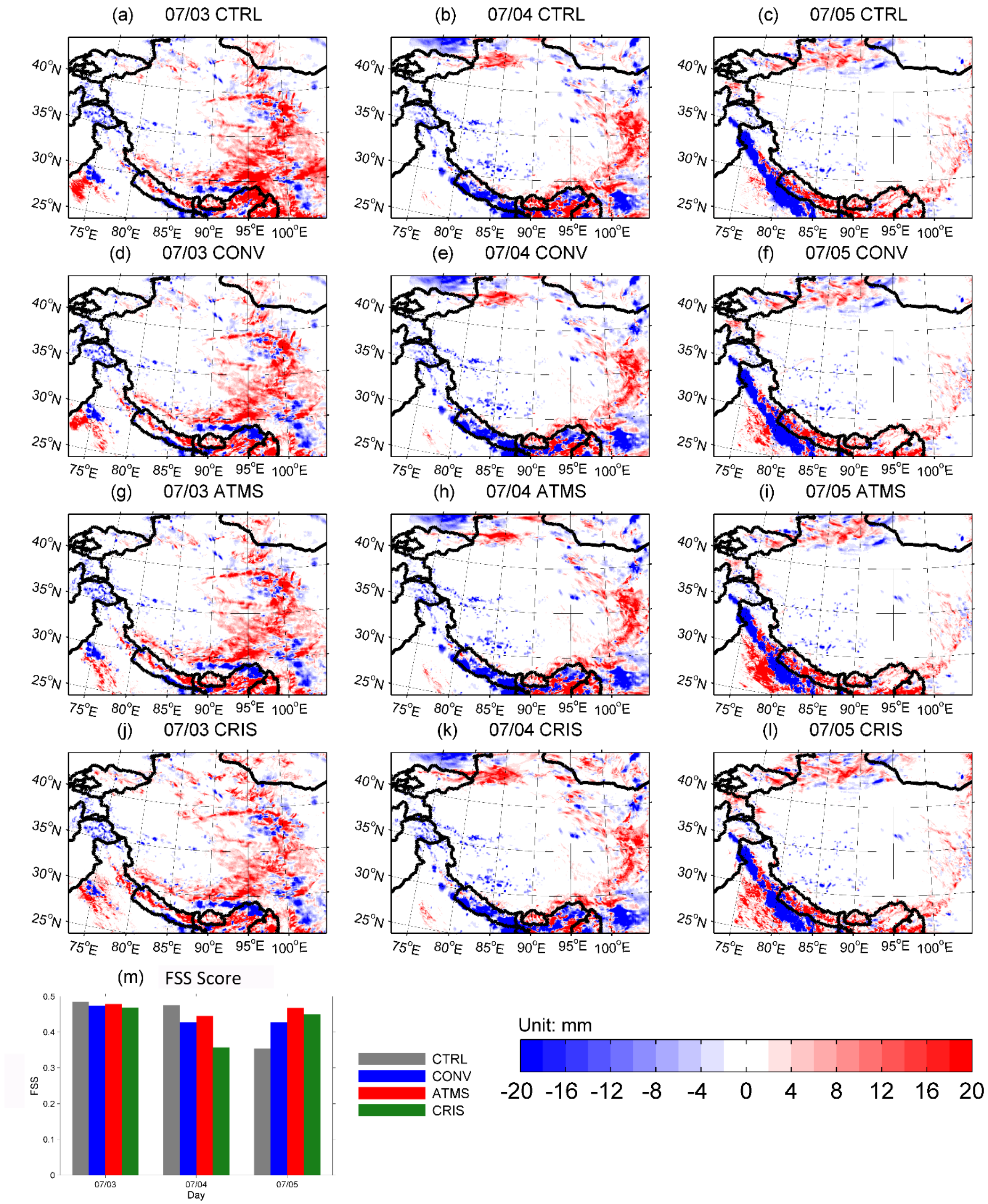

Figure 11. (a)–(l) are differences between the simulated F24H precipitation and the observed distribution and (m) is the FSS skill scores with 8 mm threshold during 3–5 July. The unit of differences is mm.